

Latent Space Imaging

Matheus Souza, Yidan Zheng, Kaizhang Kang,
Yogeshwar Nath Mishra, Qiang Fu, Wolfgang Heidrich

Visual Computing Center, King Abdullah University of Science and
Technology, Thuwal, 23955, Makkah, Saudi Arabia.

Contributing authors: matheus.medeirosdesouza@kaust.edu.sa;
yidan.zheng@kaust.edu.sa; kaizhang.kang@kaust.edu.sa;
yogeshwar.mishra@kaust.edu.sa; qiang.fu@kaust.edu.sa;
wolfgang.heidrich@kaust.edu.sa;

Abstract

Digital imaging systems have classically been based on brute-force measuring and processing of pixels organized on regular grids. The human visual system, on the other hand, performs a massive data reduction from the number of photo-receptors to the optic nerve, essentially encoding the image information into a low bandwidth latent space representation suitable for processing by the human brain. In this work, we propose to follow a similar approach for the development of artificial vision systems.

Latent Space Imaging is a new paradigm that, through a combination of optics and software, directly encodes the image information into the semantically rich latent space of a generative model, thus substantially reducing bandwidth and memory requirements during the capture process.

We demonstrate this new principle through an initial hardware prototype based on the single pixel camera. By designing an amplitude modulation scheme that encodes into the latent space of a generative model, we achieve compression ratios from 1:100 to 1:1,000 during the imaging process, illustrating the potential of latent space imaging for highly efficient imaging hardware, to enable future applications in high speed imaging, or task-specific cameras with substantially reduced hardware complexity.

Keywords: Computational Imaging, Generative Models, Single Pixel Imaging

1 Main

Conventional imaging systems are based on the brute-force sampling of scene information on regular grids. Biological vision systems operate very differently: for example the human visual system has around 120 million rods and 7 million cones [1], but the information from these photoreceptors is distilled by retinal processing into neural signals that are transmitted over the optic nerve with only 0.7-1.7 million axions [2]. This compression forms an encoding of the image information into a latent space that is compatible with the neural architecture of the human brain.

Here we propose Latent Space Imaging (LSI), a new paradigm that aims to bring this concept to the realm of cameras and artificial vision systems. Specifically, we propose to utilize the combination of linear optical encoding for drastic data reduction, paired with a small amount of non-linear computational processing to directly encode image information into the latent space of a generative model. Overall, this combination drastically reduced the amount of sensor data that needs to be captured relative to a conventional 2D image sensor.

Latent Space Imaging builds and improves upon the recent trend for co-designing both optics and reconstruction algorithms. This joint optimization has yielded favorable outcomes in computational imaging and downstream computer vision tasks. These include color image restoration [3], microscopy [4–6], monocular depth imaging [7–10], super-resolution, extended depth of field [11, 12], time-of-flight imaging [13], and high-dynamic range imaging [14], among others. The enhancements observed are attributed to the ability of such systems to *optically encode* relevant scene information into sensor data, with the computational post-processing acting as a decoder. The crucial innovation in LSI is that the code represents the rich latent space of a generative model, with that model acting as the decoder module.

While there are a number of possible ways to optically implement the LSI paradigm, our first prototype utilizes the single-pixel imaging (SPI) concept [15–18].

SPI was originally developed under the Compressed Sensing (CS) framework [19], and indeed LSI and CS share the common goal of pre-sensing data reduction. However, where CS utilizes a generic (usually random) encoding of the image, LSI uses codes that are specifically designed to embed the image into the rich latent space of a generative model in the form of a StyleGAN [20–22]. StyleGANs are renowned for their ability to synthesize highly realistic face images, editing and image-to-image translation applications. This capability stems from their semantically rich, disentangled, well-behaved, and *compact* latent space, making them an ideal architecture for LSI.

To showcase our framework, we tackle the particularly challenging task of full image reconstruction of human faces with the aim of accurate identity retrieval. Considering the distinctiveness of facial features, which present considerable challenges for existing compressed imaging techniques state-of-the-art usually suffer from blurred features and an overall loss of detail. LSI on the other hand consistently produces detailed, aesthetically pleasing faces that remain true to the original signal. Our experiments on this particularly challenging task illustrate potential for even higher compression ratios in easier tasks such as object detection or classification. Overall, the simplicity of LSI offers vast potential for expansion across a broad spectrum of applications in computer vision.

2 Results

2.1 Latent Space Imaging

Traditional imaging captures a regular $m \times n$ grid of measurements (Fig. 1a), while Compressed Sensing (CS) uses a collection of random linear codes to leverage the information redundancy inherent in real images (Fig. 1b) in combination with a reconstruction software module. In contrast, we demonstrate that meaningful information can be significantly more compressed in the latent space of generative models (Fig. 1c). Our method allows for direct imaging into this space, achieving high quality image

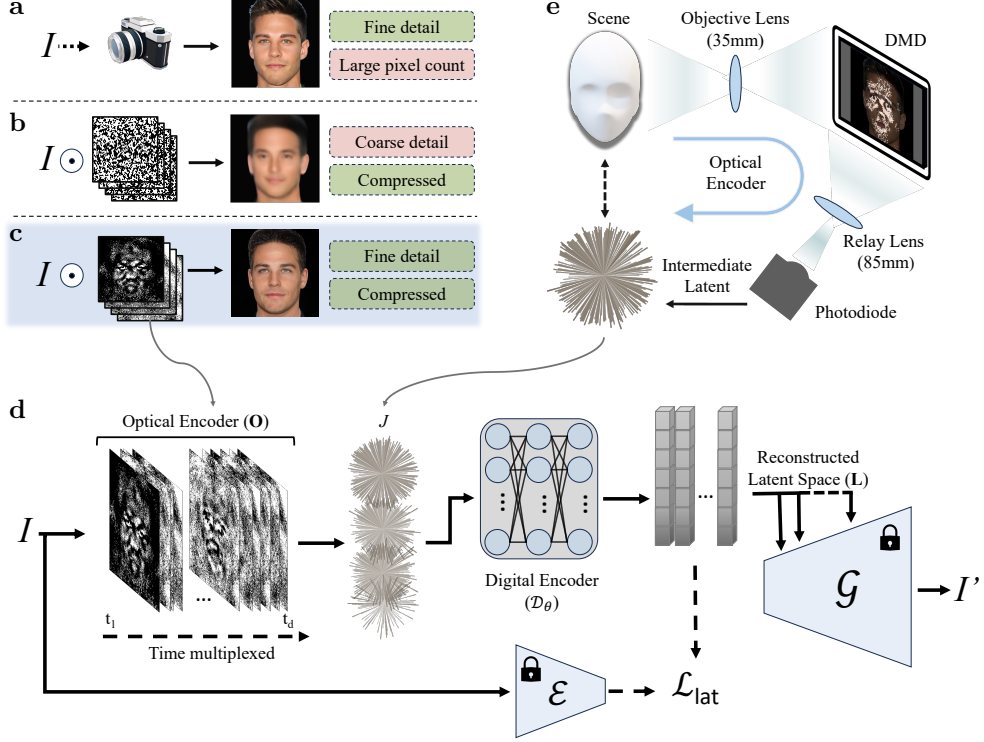


Fig. 1 (a) Traditional imaging methods require a large number of measurements and sensors with extensive pixel counting capabilities. (b) Compressed sensing techniques typically act as low-pass filters, and when the measurements are compressed below 1% of the original pixel counting they fail to reconstruct highly detailed images, even with the aid of sophisticated deep neural networks during the reconstruction process. (c) By encoding the image signal into the latent space of a generative model, surprisingly high compression rates can be achieved, while maintaining distinct fine details. (d) A linear optical and a non-linear digital encoder are jointly optimized to acquire compressed data, and encode it into the latent space provided by the inversion network \mathcal{E} by minimizing the loss function \mathcal{L}_{lat} . During reconstruction, the compressed data is fed into the generative model \mathcal{G} (StyleGAN2) in order to reconstruct the image. The *lock* symbol represents a fixed model that is not being optimized. (e) We illustrate one possible implementation of the Latent Space Imaging technique using a single-pixel framework. An objective lens focuses the image onto the Digital Micromirror Device (DMD), which is responsible for implementing the learned mask to spatially modulate the incoming signal. This is followed by a relay lens, which focuses the modulated signal onto a photodiode (SPD) responsible for integrating the signal. Utilizing time multiplexing, we can retrieve the necessary measurements.

reconstructions from only 1.0% to 0.1% of the measurements compared to the original pixel count. Unlike traditional approaches that learn to interpolate missing information, LSI enables detailed reconstruction focusing on the extraction of key domain features through a combined optical and digital encoding process.

As depicted by Fig. 1d, our objective is to learn an optically encoded mapping

$$\mathbf{L} = \mathcal{D}_\theta(\mathbf{O} \cdot I), \quad (1)$$

where the input image $I \in \mathbb{R}^{mn}$ is mapped to a tensor $\mathbf{L} \in \mathbb{R}^{k \times l}$ representing the latent space of a generative model. This mapping is achieved through the combination of a co-designed (linear) optical encoder $\mathbf{O} \in \mathbb{R}^{mn \times d}$ and a digital (nonlinear) encoder \mathcal{D}_θ , with θ representing the set of parameters that configure the digital encoder.

The optical encoder linearly projects the image to an intermediate vector $J \in \mathbb{R}^d$ representing the actual measurements of the signal, where d is 100 to 1000 times smaller than the pixel count mn in the original image. This substantial compression ratio is achieved by optimizing the projection alongside other components during the image reconstruction process. Instead of merely matching pixel values, the process targets the generative model’s latent representation \mathbf{L} of the original signal. By focusing on this compressed space, the essential features of the data distribution within a particular domain are captured, effectively eliminating redundancies inherent in the data.

However, due to the complex non-linear operations intrinsic to generative models and the impracticality of realizing these non-linearities optically, an additional digital encoder \mathcal{D}_θ is necessary to align J with the entire latent space of interest. This alignment is achieved through a deep neural network (DNN), which enhances the representation by effectively addressing the non-linearities.

The digital encoder \mathcal{D}_θ (see Fig.1d) expands J to $\mathbf{L} \in \mathbb{R}^{512 \times 18}$, aligning it with the chosen generative model’s dimensionality. In our work, StyleGAN2 [21] is employed since it performs robustly within specific domains, and its mechanisms for inversion to latent space are well-studied [23].

The digital encoder employs a multi-level network inspired by advancements in the inversion domain [24]. This approach leverages the detailed structural levels of StyleGAN2 [21]. In this framework, the optically encoded vector J passes through a series of linear layers and attention mechanisms, each followed by activation functions. The depth of these stacks varies to match the required level of detail. For the pre-trained StyleGAN2 on human faces, there are 18 levels corresponding to different resolutions. The number of stacks increases progressively from coarse to fine, aligning with low to high resolutions, respectively.

After acquiring all detail levels, we obtain $\mathbf{L} \in \mathbb{R}^{512 \times 18}$. A mixer block is then used to learn a weighted mixture of information across these levels, which is subsequently fed into the generative model \mathcal{G} to output the image I'

$$I' = \mathcal{G}(\mathbf{L}), \quad (2)$$

where $I' \in \mathbb{R}^{mn \times 3}$, with m and n determined by the capabilities of the generative model \mathcal{G} . The value 3 corresponds to the RGB color channels which are discussed in further detail later in this section.

A pivotal aspect of the LSI framework is the identification of the optimal latent space to serve as ground-truth during the optimization process. To accomplish this, we employ a pre-trained encoder, \mathcal{E} , following the method proposed by [24] for accessing the StyleGAN2 latent space. This encoder provides an approximate ground-truth latent representation, $\mathcal{E}(I)$, which serves as the target for optimizing each entry of the \mathbf{O} matrix and the \mathcal{D}_θ . The optimization is driven by the loss function \mathcal{L}_{lat}

$$\mathcal{L}_{lat} = \|\mathcal{D}_\theta(\mathbf{O} \cdot I) - \mathcal{E}(I)\|_1 \quad (3)$$

Making the encoding \mathbf{L} close to $\mathcal{E}(I)$ guarantees that it is inside the StyleGAN average space and diminishes hallucination caused by only matching an ℓ_2 norm at the

pixel image level. To further enhance facial fidelity, we incorporate additional loss functions. Detailed information on these loss functions can be found in the supplementary material.

Fig. 2a showcases the identity preservation capabilities of our model reconstructing images at a resolution of 256×256 with 256 measurements. Latent Space Imaging is able to retrieve eye colors, expression, shape, skin tone with less than 0.4% of the original pixel count. This is achieved by designing \mathbf{O} to retrieve specific features from the domain that we are targeting, thus pushing it to focus on more important characteristics on facial identification as well as the landmarks present in the underlying distribution learned by the generative model. This property, together with compressing the target space to be flat, drives the reconstruction process to not only interpolate under-sampled information but to produce an output close to the original detailed face.

Direct learning in the latent space is also an efficient method for handling color images, compared with traditional compressive sensing designs. In this approach, color is already implicitly represented in the latent space and does not require explicit modeling. \mathbf{O} integrates the signal over the wavelengths to generate our measurement, which in simulation means to sum over the RGB channels. Typically, explicit modeling would increase the number of measurements necessary for reconstruction or necessitate some trade-off between spatial and spectral resolution. Latent Space Imaging (LSI) effectively bypasses these complexities, enabling going to further compressive levels utilizing only 512, 256, 128, and 64 measurements. Fig. 2b provides an example of detailed presence even in such critical situations. This contrasts with traditional compressive sensing strategies, where limited measurements lead to reconstruction algorithms over-smoothing the images, resulting in the loss of critical identity features such as the shape of eyes, beards, and other distinguishing landmarks. Fig. 2c provides visual evidence of this phenomenon, while Fig. 2d quantitatively demonstrates

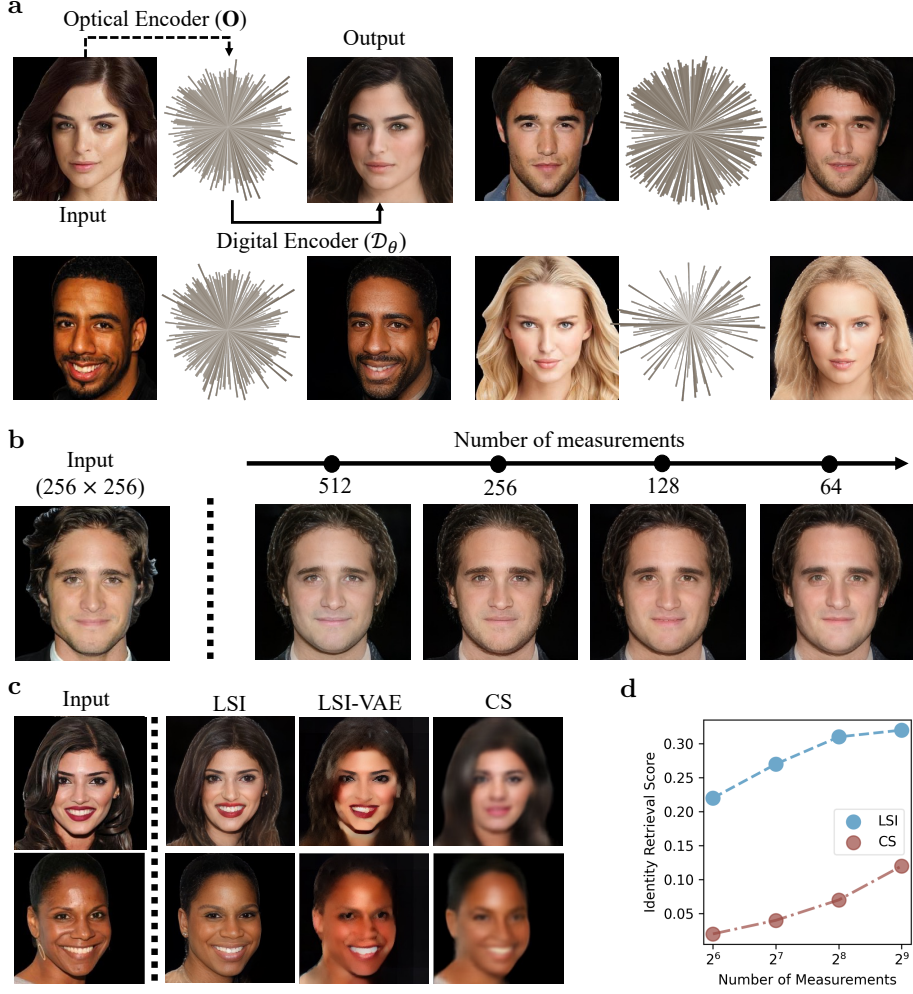


Fig. 2 (a) Simulated results of our framework compared to the ground truth. The process involves optically encoding input images using learned masks. The resulting intermediate latent space vector is visualized through the “sea urchin” diagram, where each spike represents one measured variable. (b) Compression efficiency of the LSI framework demonstrated through side-by-side comparisons. The left side of the panel shows the ground truth, while the right side illustrates the progression from 512 to 64 measurements, representing compression rates from approximately 0.8% to 0.1% of the total pixel count. (c) Visual comparison across different imaging strategies: the input image, LSI, LSI with Variational Autoencoder (LSI-VAE), and a representative method from Compressive Sensing (CS) employing Fourier Single-Pixel Imaging (FSI). The FSI image is reconstructed using a deep learning algorithm from the AuSamNet [25] framework for fixed circular mask. This panel highlights the effectiveness of our imaging strategy in retrieving detailed features. (d) Quantitative comparison of identity retrieval capabilities between LSI and CS, using is the dot product between features extracted from CurricularFace [26], a specialized model for face recognition. This plot shows that LSI excels in high-compression settings but saturates at lower ratios, whereas CS exhibits poorer performance at extreme compression levels but improves substantially as the number of measurements increases.

the differences. In this analysis, we compare Latent Space Imaging (LSI) against two other methods: LSI with a Variational Autoencoder (LSI-VAE) and Fourier Single-Pixel Imaging (FSI) [18]. For the FSI, we employ fixed circular masks coupled with a deep learning model for signal reconstruction, adhering to the procedures set forth in Huang et al.[25]. Detailed methodologies and additional comparisons are elaborated in supplementary material.

2.2 Physical Setup

Realizing the LSI framework involves implementing the optical encoder hardware along with the digital encoder software module. Among a range of different alternatives, we opt for the single-pixel camera approach as the hardware framework for our prototype. In this context, \mathbf{O} spatially modulates the incoming image I through matrix multiplication (denoted by \cdot in Equation 1). Each row of the optical encoder corresponds to a learned mask, and each column represents one measurement.

Utilizing the straight-through estimator (STE) [27], we enable the gradients to update the optical encoder, tailoring it for specific feature extraction while ensuring its physical viability. This involves maintaining \mathbf{O} 's entries as positive, bounded between $[0, 1]$, and quantized. To enhance the system's light efficiency and control over subtle changes, an energy efficiency loss is strategically added during the later stages of training. This key adjustment finely tunes the encoding process, ensuring each pattern is distinctly counted, thereby boosting the system's capability to discriminate between different patterns effectively. As demonstrated in Fig.3a, with the energy loss applied, the histogram showcases a broad spectrum of occupancies, reflecting a high diversity of patterns. In contrast, without this modification, the patterns are more uniform in their occupancy levels, exhibiting less variability. Additionally, Fig.3b illustrates that the masks projected onto the DMD following this loss application result in patterns that strikingly resemble faces, highlighting the system's focus on facial landmarks for

specific domain encoding. This enhancement not only augments detection capabilities but also prevents minor intensity changes in the projected image from going unnoticed.

To experimentally verify Latent Space Imaging, we constructed a proof-of-concept setup as depicted in Fig. 1a. In this setup, a scene is projected onto a Digital Micromirror Device (DMD TI DLP4500) using an objective lens. The image is then spatially modulated by the optimized patterns. The modulated output is captured by a relay lens, which focuses it onto a single-pixel detector (ThorLabs PDA100A2). This detector acts as an integrator, measuring a single value that represents the integrated intensity of the entire modulated image. A computer controls and synchronizes the operation of the DMD and the measurement signals, enabling the time-multiplexing of all measurements that compose the compressed signal.

Fig. 3c demonstrates the reconstruction quality of our experimental setup using a monitor as the source image. For such a task, we utilized the LSI trained to reconstruct images based on 256 measurements. We fine-tuned our model with 200 images from the FFHQ dataset, and used 100 unseen images from CelebAHQ to validate our results. This step accounts for non-modeled noise and sensor non-linearities. More details on the supplementary material.

3 Discussion

Compared to other imaging techniques, Latent Space Imaging (LSI) offers substantial benefits in domain specific scenarios with tight requirements for hardware complexity, memory and bandwidth requirements, or frame rate. As Fig. 2b illustrates, LSI is capable of keeping details even in a compression ratio 1:1,000, represented by the 64 out of 65536 measurements case, where the overall facial structure, expression, eyes and skin are well preserved.

The LSI reconstruction power inherits the advantages of a well-trained generative model specialized in a specific domain. In this approach, we leverage a pre-trained

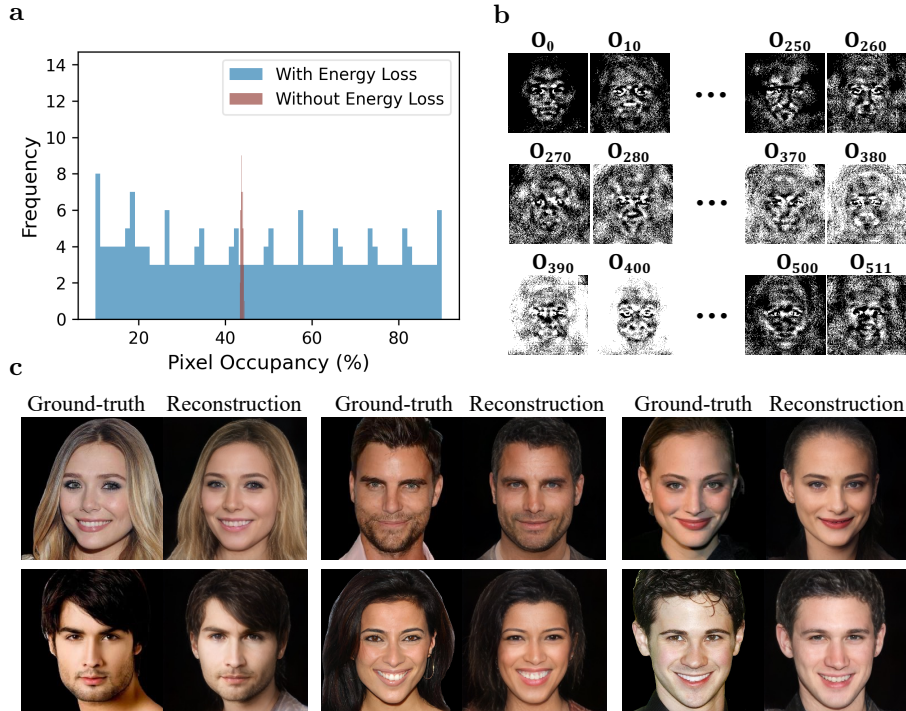


Fig. 3 (a) Shows the histogram of pixel occupancy, comparing scenarios where the energy loss function is and is not utilized. The use of energy modeling enhances the dynamic range of the measurements captured by the single sensor. (b) Displays representative patterns after using the energy loss function. (c) Demonstrates real-world captures using the setup depicted in Fig. 1c. These images are acquired with only 256 measurements, which constitutes merely approximately 0.4% of the total pixel count, based on an image resolution of 256×256 .

StyleGAN2, optimized to cover the entire distribution of the dataset. Consequently, its latent space learns to represent the most meaningful and essential information within this domain. This capability enables high-quality measurements with high compression ratios. However, it also inherently possesses the limitations of the underlying generative model and the inversion network.

Therefore, the model may fail to reconstruct very specific features not present during training, such as hats, glasses, makeup, or other distinct image details, and may struggle to generalize to a multi-domain approach. Additional analysis about challenging scenarios and how different generative models can be utilized on our framework can be found at supplementary materials.

3.1 Alternative Physical Implementations

In our prototype, we showcase the physical implementation using binary structural masking with a Digital Micromirror Device (DMD), where the light source is a monitor projecting the images. The SPI framework is an established platform for prototyping and testing different compressed imaging approaches, since the DMD acts as a programmable encoding element, making it easy to experimentally validate different code patterns and compression ratios.

However, SPI also has several downsides that limit its practicality for real imaging systems, including its form factor, and, most notably, its difficulty in dealing with moving scenes. However, the recent efforts in optical computing [28] have resulted in a range of alternative options for implementing the required optical encoding layer. For example diffractive optical elements have been used to implement both convolutional [29] and fully connected linear layers [30], and meta-surfaces have been demonstrated for shift variant convolution kernels [31]. Due to the linear nature of light, all these methods are fundamentally limited to linear operators. However, as we show with the SPI setup, linear optical encoders are sufficient for achieving high compression rates when combined with a small digital encoder. As such, any of the recently proposed optical compute frameworks could be used instead of the SPI framework, although typically this would require “freezing” the optical encoder into hardware. Nonetheless, for special purpose imaging systems, such an approach could present a more practical avenue than the SPI framework.

3.2 Relationship to Biological Vision

As mentioned in the introduction, LSI is inspired by biological vision, in particular the human visual system (HVS). Specifically, in the HVS, photoreceptors sense the spatial distribution of light, retinal ganglion cells (RGCs) encode these spatial distributions into a compressed latent space transmitted over the optic nerve, and finally the visual

cortex decodes and processes the information. LSI can be seen as analogous to this process: in our single pixel camera setup, the pixels of the spatial light modulator take on the role of the photoreceptors – they define the spatial resolution of the sensed image. The optical codes shown on the SLM, combined with the digital encoder take on the role of the RGCs, and both encode and compress this information, while the StyleGAN takes on the role of the visual cortex.

The encoding module is therefore composed of a combination of a (linear) optical computing part and a non-linear digital encoder. The digital encoder is needed since optical computing [28] is in practice limited to linear operators. Nonetheless, our work shows that even with linear optical computing, data reduction in the range of 100:1 to 1,000:1 is feasible even for the challenging task of full image restoration. Easier tasks such as object detection or classification will likely be possible with substantially higher compression ratios.

4 Future Potentials of LSI and Conclusion

Latent Space Imaging provides a general framework for imaging within a compressed environment, but its utility is not limited to this application alone. This technique opens up new avenues for exploring deeper interactions and potential innovations in image processing and analysis.

Previous studies have delved into the semantics within GAN models, uncovering boundaries in the latent space that distinguish various image attributes [32–34]. Direct visualization of these models’ latent spaces allows for a natural observation of these structures, offering significant advantages for various applications without the need for additional complex deep learning frameworks to extract these semantics.

To further investigate this, we analyzed the latent space representation \mathbf{L} of each image in the CelebA-HQ [35] test set using our pipeline, along with images I' reconstructed by StyleGAN2. We performed UMAP [36] feature reduction to visualize them

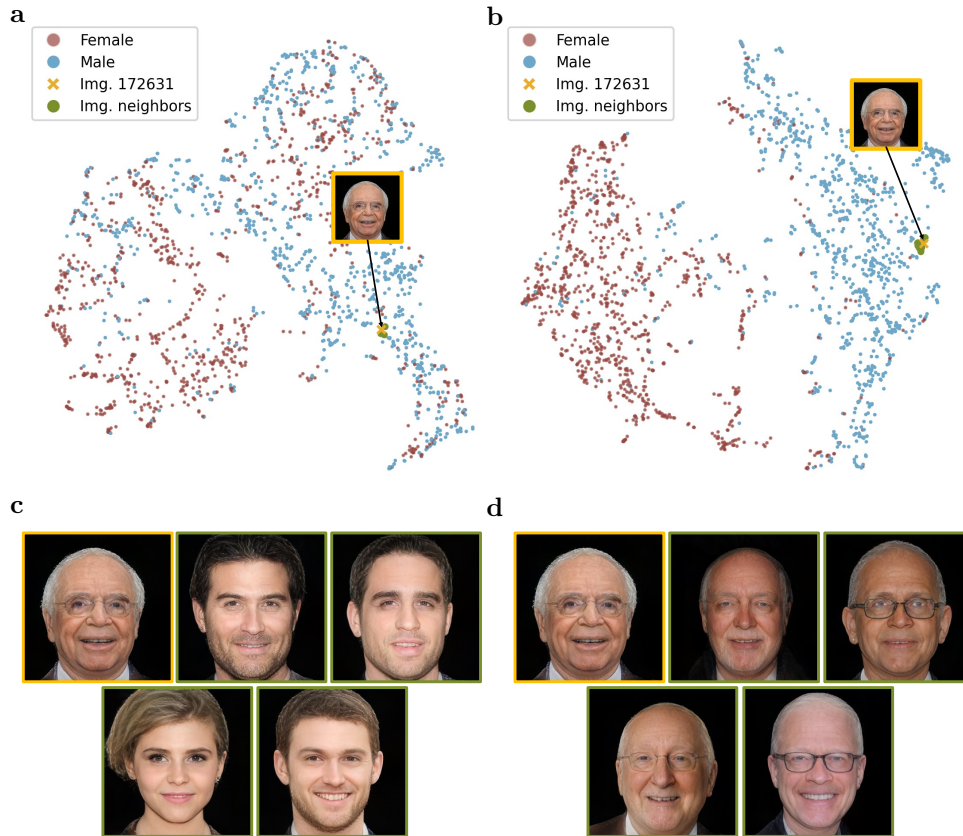


Fig. 4 Visualization of image and latent space representations using UMAP. (a) UMAP projection of images reconstructed by our pipeline, using images from the test set of CelebA-HQ, colored by gender and highlighting the image 172631 and its neighborhood. (b) UMAP projection of the corresponding latent space representations, colored by the same categories. (c) Visualization of the chosen image in the image space with its four closest neighbors. (d) The same example image with its four closest neighbors in the latent space, highlighting stronger semantic similarities among neighbors. We fit the UMAP for 5 nearest neighbors for each point, with a small minimum distance of 0.001 to ensure that points are tightly packed, preserving local relationships and creating distinct clusters.

in a 2D map. Fig.4a shows the image representation, while Fig.4b illustrates the latent space representation.

The latent representation forms clusters based on image features. For instance, we highlighted males, females, and one specific image along with its neighborhood in different colors. Males tend to cluster on one side, separated from females, and image 172631 clusters close to images with similar characteristics (e.g., hair color,

age, glasses, skin tone). This clear semantic division is not observable in the image-based representation. To illustrate this, we examined the four closest neighbors in each representation. It is evident that the neighbors in the latent space share more semantic similarities (see Fig. 4c,d).

This analysis not only underscores that latent space representations enable a novel compressed imaging process, but also demonstrates their potential as powerful semantic extractors. Such capabilities suggest that exploring these representations could yield significant insights and advancements in the field of generative models, potentially leading to more effective and nuanced image processing techniques in the future.

Besides a semantic analysis, the LSI framework here leverages a single-pixel approach. This implementation can be engineered for high frame rate due to low bandwidth requirements, and utilizing state-of-the-art DMDs would provide an out-of-box improvement for the already proposed setup. As discussed, Latent Space Imaging (LSI) could also be effectively implemented using a variety of other optical computing paradigms, such as diffractive optical elements and meta-surfaces (see Sec.3.1). These alternatives to the traditional Single Pixel Imaging (SPI) framework can manage optical encoding with high efficiency. Furthermore, enhancing the digital decoder through research into different generative model implementations holds promise for significantly improving both the versatility and efficacy of LSI systems. This approach could lead to more practical and adaptable imaging solutions, particularly suited for dynamic environments.

5 Methods

We utilized PyTorch to design and validate the LSI framework. All training details, hyperparameters and \mathcal{D}_θ architecture detailed description and discussion can be found in the supplementary material.

5.1 Optical Encoder Optimization

In the \mathbf{O} optimization process, we employ the straight-through estimator (STE) [27], a technique also favored (VQ-VAEs) [37–39]. During the forward pass, values are quantized and constrained before computing J . However, during back-propagation, gradients are allowed to flow through the non-quantized version, facilitating weight updates. Importantly, we ensure that the entries of \mathbf{O} remain positive and are bounded between $[0, 1]$. Although using complementary patterns [40] allows for the inclusion of negative values, empirical experiments have shown that this approach does not yield significant improvements and necessitates double the measurements.

Initially, masks are generated from a uniform distribution and are then binarized through a quantization process. This process results in binary patterns that achieve an even total counting of 0s and 1s, theoretically maximizing bit entropy and steering the system towards an optimal solution [41]. This distribution presumes the sensor is sensitive enough to discern very fine differences, a demanding prerequisite as each pattern will have similar total intensity. This issue is addressed using the energy loss mechanism, which was introduced in Section 2.2 and is further detailed in the supplementary material.

5.2 Digital Encoder Optimization

Inspired by inversion networks, our approach tailors the digital encoder specifically for our unique imaging task. Unlike traditional inversion processes used for image editing, our encoder is designed for an optically compressed inversion, aligning the characteristics of the latent vector with the optical system’s constraints. This method allows our encoder to generalize across any image within the domain, without the need for training on specific data points.

In the broader context of the traditional inversion process, a latent array is retrieved from a pre-trained generative model to accurately reproduce the original image. This

enables not only spatial adjustments, such as translation and rotation, but also semantic modifications including age, hair color, and expression changes. The inversion can be achieved through various methods: it may involve a full optimization for each data point [21, 42, 43], the use of an encoder trained to produce latent representations in a zero-shot manner [24, 44], or a combination of these strategies [45–47].

5.3 Datasets

To effectively exploit the latent space of generative models, we have narrowed our focus to the domain of human facial recognition. Specifically, we aim to retrieve identities from pictures of human faces. For this purpose, we utilized two datasets: FFHQ [20] and CelebAHQ [35]. The FFHQ dataset was exclusively employed for training, while CelebAHQ was used both for training and testing—comprising 28,000 images for training and 2,000 for testing. Combined with FFHQ, this resulted in a total of 98,000 face images used for training. This approach ensures a robust dataset that enhances the reliability and effectiveness of our model in capturing and reconstructing facial identities.

Both datasets contain background information that could pose a challenge due to the already compressed measurements. To address this, we further refine the domain by applying Segment Anything (SAM) [48] to remove background elements and prioritize identity retrieval. Moreover, the versatility of LSI allows it to be easily extended to other specific domains by adopting generative models trained on different datasets.

6 Code Availability

The code will be made available together with all checkpoints to ensure reproducibility.

7 Data Availability

The CelebA-HQ dataset is accessible on GitHub at https://github.com/tkarras/progressive_growing_of_gans. The FFHQ dataset can be found at <https://github.com/NVlabs/ffhq-dataset>. The AFHQ can be obtained at <https://github.com/clovaai/stargan-v2/tree/master>.

Supplementary Material

S1 Digital Encoder Architecture

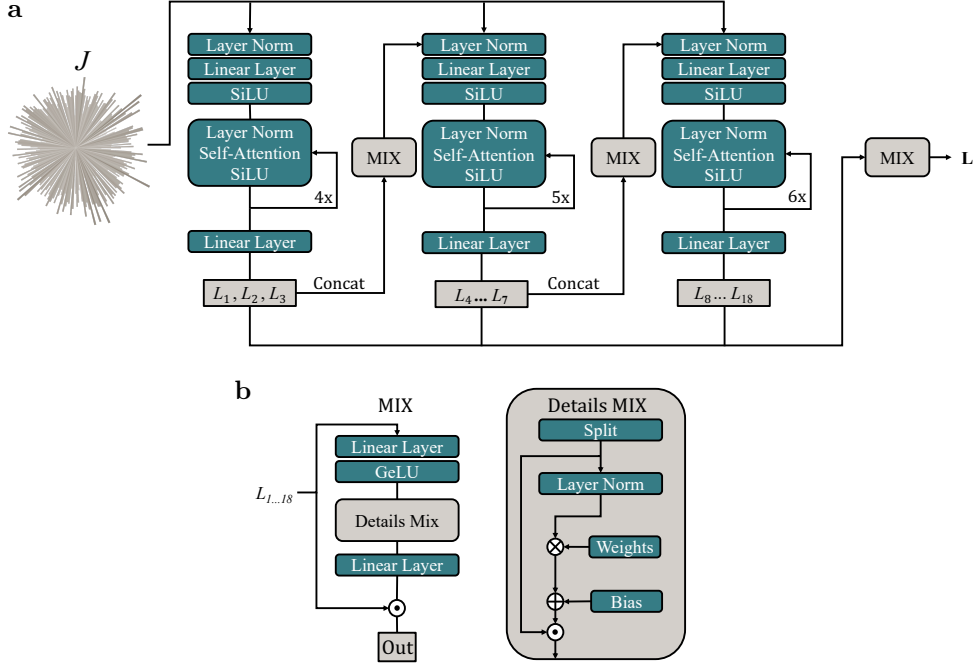


Fig. S1 (a) Overview of all the blocks involved in the digital encoder architecture. The three steps capture coarse, middle, and fine details, with each step depending on the output of the previous one. (b) Illustration of the MIX process. The latent vector is statically projected to capture interactions among different levels of detail.

After acquiring the measurements J from the co-optimized optical encoder \mathbf{O} , we employ a digital encoder network \mathcal{D}_θ . The objective of this model is to match the intermediate latent space produced by the measurements with the actual latent able to reproduce the image of interest I .

The original StyleGAN2 implementation receives a random noise vector $Z \in \mathbb{R}^{512}$ and utilizes a mapping network to project this to different levels of details, result in

$\mathbf{L} \in \mathbb{R}^{512 \times l}$, l may vary depending the desired image resolution that the generative models was trained to generate. In the case of face images, l is equal to 18, finally we want \mathbf{O} to map $J \in \mathbb{R}^d$ to $\mathbf{L} \in \mathbb{R}^{512 \times 18}$. d corresponds to our measurement count, therefore, going from 512 to 64.

As depicted by Fig. S1a, the intermediate latent goes first through 3 different set of blocks from left to right. The first one produce the first 3 elements of \mathbf{L} out of 18, each one of them only take into account the initial J . The middle block, besides J , it also takes the concatenation of L_1, L_2 and L_3 through the MIX module, as input, outputting L_4 to L_7 . Finally, the last block follows the same idea, it concatenates the output of the middle one and pass through another MIX block, the output of this is summed together with the original measurement and it passes through the block to finally result in L_8 to L_{18} . The idea here is to make the optical-aware inversion network match the multi-level structure of StyleGAN2, following a coarse-to-fine approach.

In the end, the latents from all detail levels pass through the MIX block. The purpose of the MIX blocks is to facilitate interactions and learn a weighted mixture across multiple detail levels. The model incorporates the spatial gating unit proposed in [49]. Within the MIX block (see Fig.S1b), the features are projected to a higher dimension, after which the resulting tensor x is split into two parts, u and v , along the channel dimension. This division allows for separate processing paths within the block. v is normalized and linearly projected using a weights matrix and bias vector to capture interactions in a static manner, as the weights matrix remains unchanged after training because it does not depend on the input. The final element-wise multiplication of u and the projected v modulates the information flow, controlling which parts of u are allowed to pass through—similar to a gating mechanism. Finally, this gated output is merged with the input through a residual connection, preserving the original information and enhancing gradient flow during back-propagation.

S2 Loss Functions and Training Details

In this work, we trained the optical \mathbf{O} and digital \mathcal{D}_θ encoders while keeping the generative model, StyleGAN2, frozen. To jointly optimize these components, we utilized an off-the-shelf inversion network pre-trained to invert images to the StyleGAN2 latent space of a specific domain [24]. This network is used to compute a latent similarity loss function (\mathcal{L}_{lat}), making the output of the \mathcal{D}_θ similar to the latent space approximated by this model. This process is described in Equation 3 of the main text.

Additionally, we aim to match the image quality at the pixel level and enforce identity similarity. For this task, we used the identity loss (\mathcal{L}_{id}), which computes the cosine distance between feature maps extracted by ArcFace [50], a facial recognition network. We also utilized the ℓ_2 norm (\mathcal{L}_{l2}) and LPIPS (\mathcal{L}_{lips}) [51] to enforce pixel-wise and perceptual similarities, respectively.

The total loss function during training can be summarized as follows:

$$\mathcal{L}_{total} = \lambda_{lat}\mathcal{L}_{lat} + \lambda_{id}\mathcal{L}_{id} + \lambda_{lips}\mathcal{L}_{lips} + \lambda_{l2}\mathcal{L}_{l2} \quad (\text{S1})$$

After convergence, we added an additional loss term ($\lambda_{energy}\mathcal{L}_{energy}$) to account for the intensity diversity among the masks.

$$\mathcal{L}_{energy} = \frac{1}{d} \sum_j^d \left| \sum_i^{mn} \mathbf{O}_{i,j} - \epsilon_j \right| \quad (\text{S2})$$

Here, ϵ represents the ground-truth energy level, heuristically designed to correspond to a certain percentage of pixels set to one. This percentage increases incrementally from 10% to 90%, with a step of 1%. The patterns are shuffled to avoid any undesired structure.

To optimize \mathbf{O} and \mathcal{D}_θ , we employ distinct optimizers: Lion [52] for \mathbf{O} and Ranger (combination of Lookahead [53] and the Rectified Adam [54]) for \mathcal{D}_θ , each with a learning rate of 10^{-4} . The weighting coefficients λ for each loss function are set at

1, 0.5, 0.8, and 1, in the respective order that they appear in Equation S1. Additionally, for the energy loss component, we set λ to 3. Regarding batch sizes, we typically use 32 for face datasets. However, for the AFHQ [55] dataset, as discussed in Sec. S4, the batch size is reduced to 8 due to the limited number of images available. For all experiments we utilize a single NVIDIA A100.

S3 Experimental setup

Our experimental setup utilizes a single-pixel imaging configuration as follows: Face images are displayed on a high-dynamic-range Eizo CG3145 monitor. These images are then focused onto the DMD of the Texas Instruments DLPLCR4500EVM evaluation board using a Canon EF 35mm f/2 IS USM objective lens. We interpolate our learned 256×256 patterns to optimally fill the largest possible area, adjusting the scale to compensate for the diamond-shaped micromirror grid of the DMD. This adjustment ensures full utilization of the height within a central square region. The DMD spatially modulates the image by reflecting patterns according to an optimized encoding matrix (**O**). The resultant patterned light is captured by a photodiode (PDA100A2) through a Canon EF 85mm f/1.8 USM relay lens. An analog-to-digital converter (NI 6001) converts the received analog signals into digital form. The digital data are then received by a connected PC, which is also responsible for synchronizing all components involved in the experimental setup.

To enhance the congruence between our measurements and simulations, we employ a white image to determine a global scaling deviation and apply a correction factor. This approach effectively reduces the gap between simulation and measurement, yet some inherent challenges persist due to non-linear behaviors, minor deviations in DMD reflection angles, and sensor noise, which complicate the precise replication of simulated conditions. However, by leveraging the controlled environment of our

experimental setup, we are able to systematically gather real-world training data and fine-tune \mathcal{D}_θ .

The fine-tuning process involves selecting a subset of 200 training images and measuring their outputs using our configured setup. We employ the loss functions specified in Equation S1, while reducing the learning rate to 10^{-5} , to optimize performance and accuracy in real-world applications. Fig. S2 illustrates the effect of fine-tuning.

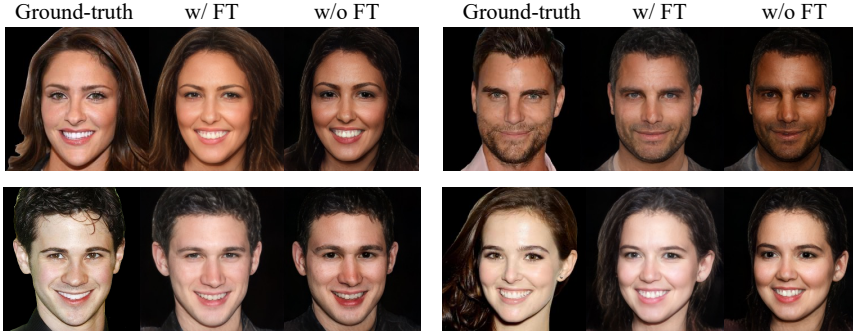


Fig. S2 Demonstrates the effect of the fine-tuning process on our model. Post fine-tuning, the average ID similarity of the 100 test images increases from 0.25 to 0.31. This enhancement brings the values in line with those observed in our simulation results, indicating a closer match and improved performance.

S4 Additional Results

We present additional LSI results encompassing a diverse set of images, along with the range of compression levels studied in this work. Our methodology involves reconstructing images with a resolution of 256×256 pixels and examining compression rates that result in retaining 512, 256, 128, and 64 total measurements.

In Fig. S3 a consistent retention of facial details is observed even with increasing compression, highlighting the effectiveness of our approach even at higher compression rates. Targeting the latent space addresses the over-smooth appearance typical of strong sub-sampling strategies, preserving textures and achieving a realistic look instead of creating flat reconstructions. Here, we emphasize the persistence of facial

expressions, with key features such as eyebrow shape, beard, and smile being well reconstructed.

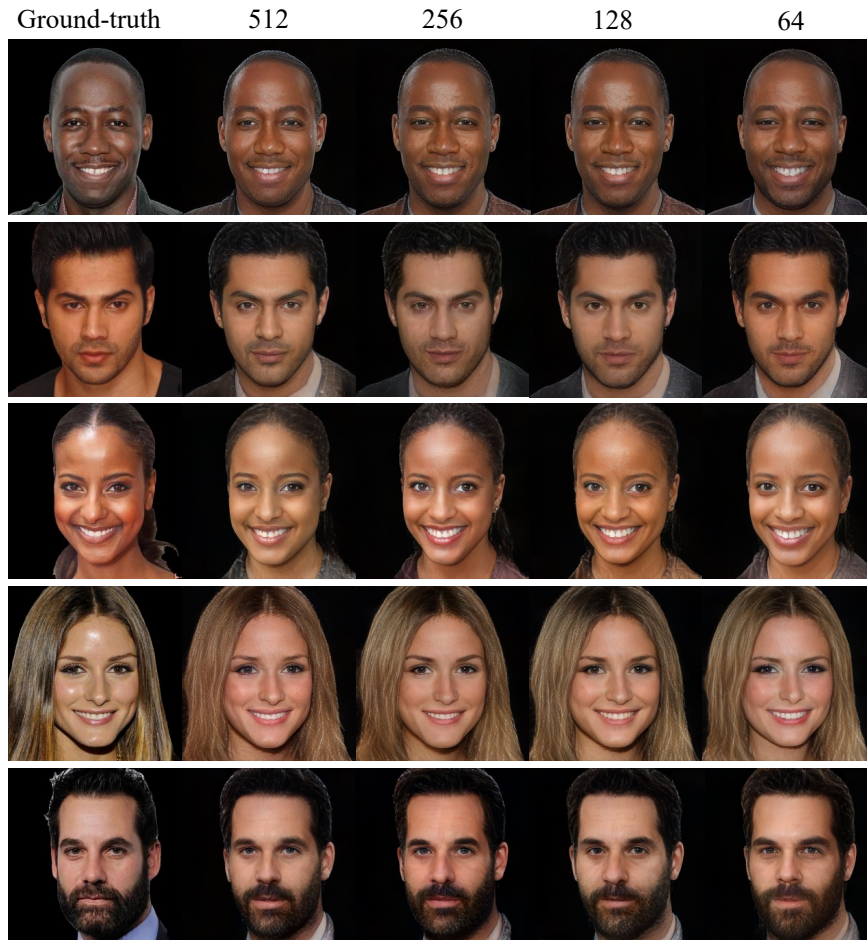


Fig. S3 Additional results for the simulation case accounting for all set of compression rates proposed in this work, 512, 256, 128 and 64 measurements which corresponds to approximately 0.8%,0.4%,0.2% and 0.1% of the total pixel count.

Additional domains were explored in Fig. S4, we utilize our simulated pipeline with 512 measurements to reconstruct cats and dogs images from AFHQ dataset [55]. These datasets imposed additional challenge because they are very small compared

with FFHQ, with only 5000 training images. However, LSI is capable to faithfully reconstruct such domain pictures.



Fig. S4 Illustrates another set of reconstructions from our simulated results, highlighting the versatility of our methods across various domains, such as cats and dogs.

In Fig. S5 we also expand the examples of reconstructions performed by our physical setup utilizing the single-pixel approach for the 256 measurements case.

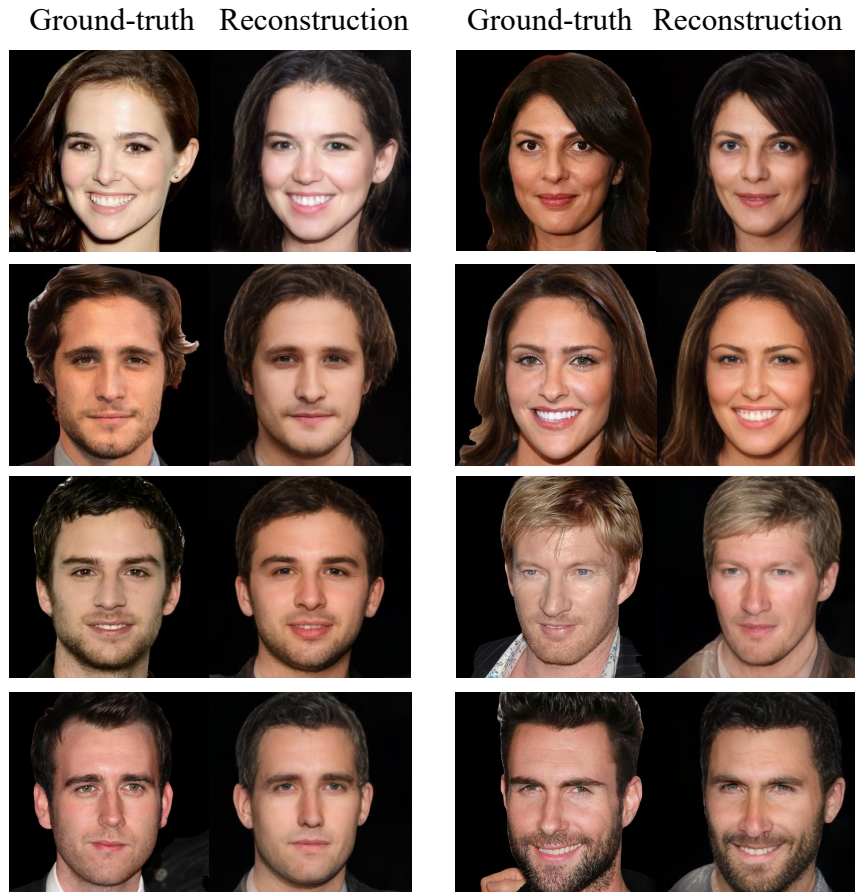


Fig. S5 Showcase another set of reconstructions performed by the proposed physical setup.

S5 Failure Cases and Limitations

As we are focusing on faces and our underlying generative model is primarily trained with frontal-centered faces under typical daily lighting, strong deviations from these conditions are not properly modeled and result in strong hallucinations. Fig. S6a shows some failure conditions. From these observations, we note that accessories like glasses and hats are not modeled by the generative model and cannot be reconstructed. Additionally, other parts of the body are also not reproducible, and faces oriented far from a frontal view add additional burden to the reconstruction process. Similar behavior is observed in other works utilizing an encoder network to perform inversion

when a purely software-based network is employed. In our case, we are dealing with a more challenging scenario where a real spatial encoder compresses the image to a very limited amount of data. Fig. S6b demonstrates how significant features can be lost in challenging scenes when compressing to over 99.9%. We notice that the mouth is not open as in the original image. This behavior can be explained by the underlying distribution learned by the generative model, where few images have the mouth in such a position. Consequently, our model struggles to reconstruct it accurately.

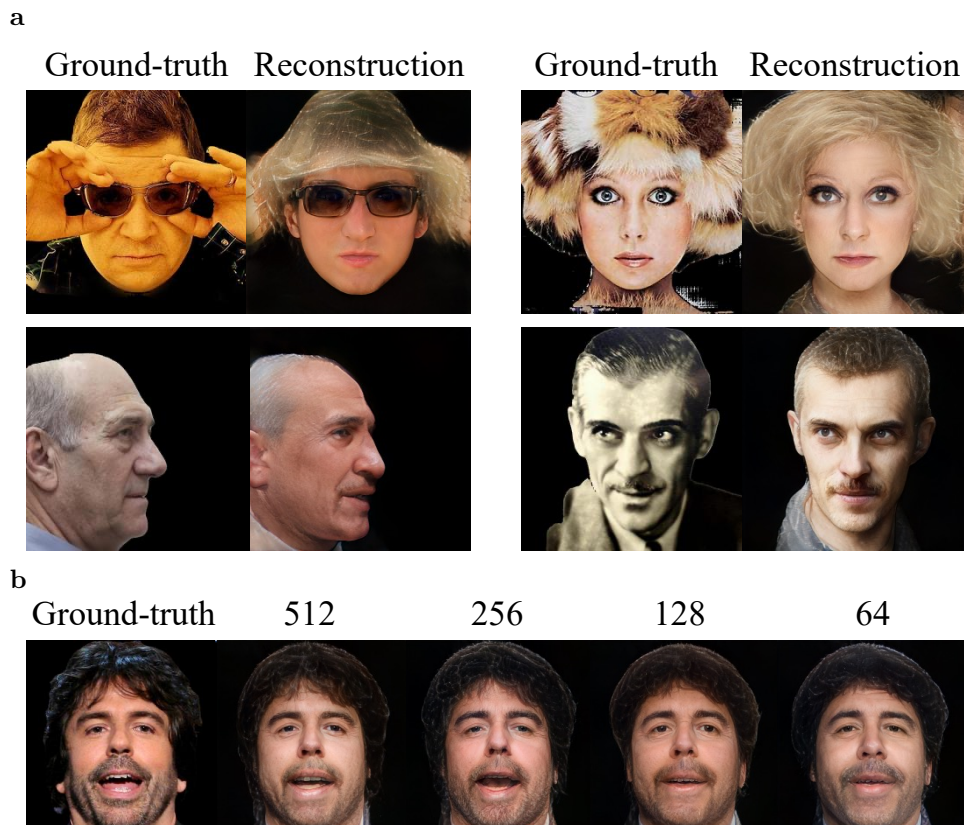


Fig. S6 (a) Illustrates the conditions where LSI fails to reproduce the scene. Demonstrate different challenging scenarios like accessories, face orientation, and color reproduction. (b) Exemplify a case where extreme compression hurt the expression reconstruction.

S6 Latent Space Image in the context of Compressive Sensing

Latent Space Imaging (LSI) aims to retrieve rich compressed information from a specific domain, directly targeting the latent space of the underlying reconstruction model. The concept can be used in different imaging modalities. Here, we showcase the compression aspect of LSI utilizing a single-pixel approach. Therefore, we compare against traditional compressive sensing (CS) strategies.

First, it is essential to state that some CS ideas in the literature are introduced only in simulation and may make unrealistic assumptions that prevent actual hardware implementation. Works like [56–59], to name a few, provide valuable insights on how to improve compressive sensing reconstructions. However, they are not applicable because they have measurement matrices that are not feasible in the real world due to negative entries, or they do not consider challenges like quantization. Here, we are interested in methods that are feasible in an experimental setup.

In this context, DCAN [60] and follow-up works optimize their binary patterns together with a deep learning model for reconstruction in the spatial domain. Other solutions shift to the Fourier domain as proposed by [18], leveraging the fact that information is usually concentrated on low-frequencies, enabling under-sampling strategies with high-quality reconstructions but suffering when dealing with low sampling rates [61]. Recent Fourier single-pixel imaging (FSI) techniques try to overcome such issue, using a more advanced network as a reconstruction method, improving the heuristics for the frequency domain filters designing and jointly optimizing the masks and reconstruction algorithms [25, 62, 63].

Finally, to assess how LSI reconstruction quality is compared with SPI, we retrain FSI models using a fixed circle mask and optimize it with the deep learning reconstruction using AuSamNet pipeline [25]. To also analyze the performance when utilizing more sophisticated deep learning strategies from a CS perspective, we retrain

SAUNet [59] imposing the quantization constraints. We train and evaluate using the same dataset as LSI and a similar compression rate.

AuSamNet and FSI-DL [25]

Both are Fourier basis methods with deep learning reconstruction algorithms; the first optimizes the mask, and the second utilizes a fixed heuristically designed circular mask. The patterns P_ϕ are generated using the ideal proposed by [18]

$$P_\phi(x, y; f_x, f_y) = a + b \cos(2\pi f_x x + 2\pi f_y y + \phi), \quad (\text{S3})$$

where (x, y) represents the 2D Cartesian coordinates in the scene, a symbolizes the average intensity distribution, b stands for the amplitude of the Fourier basis pattern, and (f_x, f_y) indicates the non-zero spatial frequency points within the optimized mask. Furthermore, ϕ denotes the initial phase, adopting three steps phase shifting of 0, $2\pi/3$, and $4\pi/3$.

This work also utilizes a color filter array (CFA) and demosaic process to reduce the number of measurements necessary to retrieve color images, computing the Fourier transform of the CFA and multiplying it with the mask.

When evaluating under our heavily compressed setting, AuSamNet cannot optimize the mask, leading to unstable results. FSI-DL is capable of reconstructing the images but produces low-quality results as demonstrated by Fig. S7.

SAUNet [59]

This approach proposes a 2D measurement system and an unfolding network as a reconstruction algorithm. Their measurement can be defined by the equation $Y = HXW^T$, where H and W are learned during the optimization process, and X is the input. To enable a fair comparison, we clamped and then quantize their measurement matrix during training to be binary, following the same procedure adopted by our

methods. We add a normalization layer after utilizing H and W to avoid exploding gradients and instability.

Similar to FSI-DL, SAUNet can reconstruct images but struggles to maintain fine details, resulting in lower quality outputs (see Fig. S7). It is important to note that we trained SAUNet following the methodology outlined in their work. Like many other compressive sensing approaches, we utilized the YCrCb color space. In this approach, the objective is to reproduce the luminance component, while the chrominance components were added during inference using ground-truth values. This approach gives them an advantage, as they would in any practical setting require additional measurements to reproduce color images or model color filters in conjunction with the modulation masks, as proposed by AuSamNet [25].

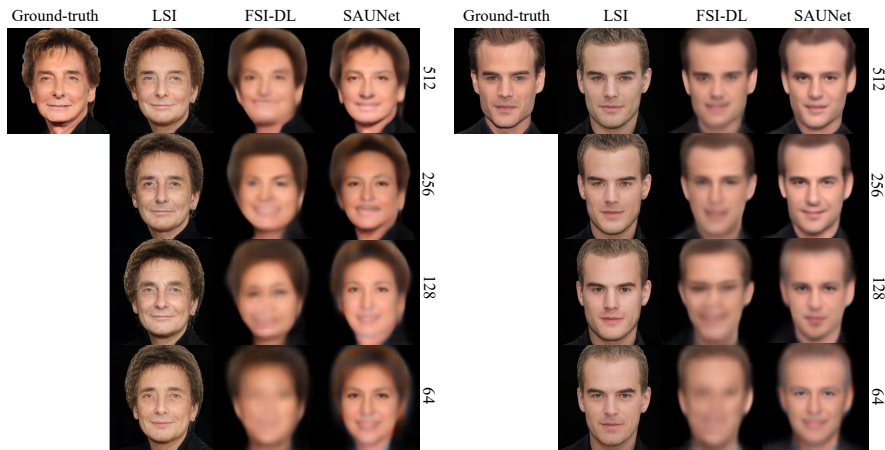


Fig. S7 LSI qualitatively compared against compressive sensing approaches across several compression ratios.

S6.1 Different Generative Models

Recent advancements in diffusion models have significantly improved the generation of high-quality, text-guided images, their success root also in leveraging the latent space [64]. This process utilizes a VAE as the encoder to the latent space and decoder

to back to image, which can also be applied in LSI. However, such generative models still depend on spatial structures, with a latent space of $4 \times 32 \times 32$ for 256×256 images. To leverage the encoding power of VAE, we replaced the StyleGAN generator with the VAE decoder and used the encoder to provide a new ground-truth $\mathcal{E}(I)$ for our target latent space, then solving the Equation 3 in the main text. The spatial structure in this latent space, coupled with its training for multi-domain applications, leads to some traditional compressive sensing issues, where high-frequency information is often lost during reconstruction (see Fig.3c in the main text). However, because our approach directly images to a compressed latent space, it outperforms other methods like Fourier single-pixel imaging. The compactness of the StyleGAN latent space exemplifies its superior suitability over VAE for the application demonstrated here.

S7 Evaluation Metrics

It is well established that traditional metrics such as PSNR and SSIM do not correlate well with human visual perception [51, 65, 66]. These metrics prioritize pixel-level accuracy and are largely insensitive to aspects of perceptual quality, failing to account for high-level structural information. Seminal studies, such as [51], have demonstrated that phenomena like blurring, which significantly impact perceptual experience, often lead to minimal changes in the L2 norm. This limitation becomes particularly pronounced in the context of heavily compressed image reconstructions, where PSNR and SSIM inadequately reflect the extent of perceived quality deterioration.

In this work, we evaluate our methods in terms of identity similarity and FID [67]. The first one, is the dot product between features extracted from CurricularFace [26], a specialized model for face recognition, which is different from the one utilized during training to compute the ID loss, in order to guarantee that we are not optimizing for specific evaluation metric.

Finally, Table S1 presents the evaluation metrics for LSI, FSI-DL, and SAUNet. It is evident that our method produces superior perceptual quality, particularly in heavily compressed cases where other methods fail entirely.

Table S1 Comparison of ID and FID scores across different methods and resolutions (top result shown in **bold**).

	512		256		128		64	
	ID \uparrow	FID \downarrow	ID \uparrow	FID \downarrow	ID \uparrow	FID \downarrow	ID \uparrow	FID \downarrow
LSI	0.32	35.57	0.31	35.65	0.27	37.19	0.22	37.29
FSI-DL	0.12	107.48	0.07	118.79	0.04	134.40	0.02	173.71
SAUNet	0.24	58.96	0.14	75.53	0.09	104.23	0.06	107.35

References

- [1] Molday, R.S., Moritz, O.L.: Photoreceptors at a glance. *Journal of Cell Science* **128**(22), 4039–4045 (2015)
- [2] Jonas, J.B., Schmidt, A.M., Müller-Bergh, J., Schlötzer-Schrehardt, U., Naumann, G.: Human optic nerve fiber count and optic disc size. *Investigative Ophthalmology & Visual Science* **33**(6), 2012–2018 (1992)
- [3] Chakrabarti, A.: Learning sensor multiplexing design through back-propagation. In: *Proceedings of the 30th International Conference on Neural Information Processing Systems. NIPS’16*, pp. 3089–3097. Curran Associates Inc., Red Hook, NY, USA (2016)
- [4] Nehme, E., Freedman, D., Gordon, R., Ferdman, B., Weiss, L., Alalouf, O., Naor, T., Orange, R., Michaeli, T., Shechtman, Y.: DeepSTORM3D: dense 3D localization microscopy and PSF design by deep learning. *Nat. Methods* **17**, 1–7 (2020)
- [5] Kellman, M., Bostan, E., Chen, M., Waller, L.: Data-driven design for Fourier

- ptychographic microscopy. In: 2019 IEEE International Conference on Computational Photography (ICCP), pp. 1–8 (2019)
- [6] Shechtman, Y., Weiss, L., Backer, A., Lee, M., Moerner, W.: Multicolour localization microscopy by point-spread-function engineering. *Nat. Photonics* **10** (2016)
- [7] Chang, J., Wetzstein, G.: Deep optics for monocular depth estimation and 3d object detection. In: Proceedings of the IEEE/CVF International Conference on Computer Vision, pp. 10193–10202 (2019)
- [8] Haim, H., Elmalem, S., Giryas, R., Bronstein, A.M., Marom, E.: Depth estimation from a single image using deep learned phase coded mask. *IEEE Transactions on Computational Imaging* **4**(3), 298–310 (2018)
- [9] He, L., Wang, G., Hu, Z.: Learning depth from single images with deep neural network embedding focal length. *IEEE Transactions on Image Processing* **27**(9), 4676–4689 (2018)
- [10] Wu, Y., Boominathan, V., Chen, H., Sankaranarayanan, A., Veeraraghavan, A.: PhaseCAM3D—learning phase masks for passive single view depth estimation. In: 2019 IEEE International Conference on Computational Photography (ICCP), pp. 1–12 (2019). IEEE
- [11] Sitzmann, V., Diamond, S., Peng, Y., Dun, X., Boyd, S., Heidrich, W., Heide, F., Wetzstein, G.: End-to-end optimization of optics and image processing for achromatic extended depth of field and super-resolution imaging. *ACM Transactions on Graphics (TOG)* **37**(4), 1–13 (2018)
- [12] Sun, Q., Wang, C., Fu, Q., Dun, X., Heidrich, W.: End-to-end complex lens design with differentiate ray tracing. *ACM Trans. Graph.* **40**(4) (2021)

- [13] Chugunov, I., Baek, S.-H., Fu, Q., Heidrich, W., Heide, F.: Mask-tof: Learning microlens masks for flying pixel correction in time-of-flight imaging. In: IEEE Conf. Comput. Vis. Pattern Recog., pp. 9116–9126 (2021)
- [14] Sun, Q., Tseng, E., Fu, Q., Heidrich, W., Heide, F.: Learning Rank-1 diffractive optics for single-shot high dynamic range imaging. In: IEEE Conf. Comput. Vis. Pattern Recog., pp. 1386–1396 (2020)
- [15] Duarte, M.F., Davenport, M.A., Takhar, D., Laska, J.N., Sun, T., Kelly, K.F., Baraniuk, R.G.: Single-pixel imaging via compressive sampling. *IEEE Signal Processing Magazine* **25**(2), 83–91 (2008)
- [16] Katz, O., Bromberg, Y., Silberberg, Y.: Compressive ghost imaging. *Applied Physics Letters* **95**(13) (2009)
- [17] Song, K., Bian, Y., Wu, K., Liu, H., Han, S., Li, J., Tian, J., Qin, C., Hu, J., Xiao, L.: Single-pixel imaging based on deep learning (2023)
- [18] Zhang, Z., Ma, X., Zhong, J.: Single-pixel imaging by means of fourier spectrum acquisition. *Nat. Commun.* **6**(1), 6225 (2015)
- [19] Donoho, D.L.: Compressed sensing. *IEEE Transactions on Information Theory* **52**(4), 1289–1306 (2006)
- [20] Karras, T., Laine, S., Aila, T.: A Style-Based Generator Architecture for Generative Adversarial Networks (2019)
- [21] Karras, T., Laine, S., Aittala, M., Hellsten, J., Lehtinen, J., Aila, T.: Analyzing and improving the image quality of StyleGAN. In: Proc. CVPR (2020)
- [22] Karras, T., Aittala, M., Laine, S., Härkönen, E., Hellsten, J., Lehtinen, J., Aila, T.: Alias-free generative adversarial networks. *Advances in Neural Information*

- [23] Xia, W., Zhang, Y., Yang, Y., Xue, J.-H., Zhou, B., Yang, M.-H.: GAN inversion: A survey. *IEEE Trans. Pattern Anal. Mach. Intell.* (2022)
- [24] Richardson, E., Alaluf, Y., Patashnik, O., Nitzan, Y., Azar, Y., Shapiro, S., Cohen-Or, D.: Encoding in style: a StyleGAN encoder for image-to-image translation. In: *IEEE Conf. Comput. Vis. Pattern Recog.* (2021)
- [25] Huang, W., Wang, F., Zhang, X., Jin, Y., Situ, G.: Learning-based adaptive under-sampling for fourier single-pixel imaging. *Opt. Lett.* **48**(11), 2985–2988 (2023)
- [26] Huang, Y., Wang, Y., Tai, Y., Liu, X., Shen, P., Li, S., Li, J., Huang, F.: Curricularface: adaptive curriculum learning loss for deep face recognition. In: *IEEE Conf. Comput. Vis. Pattern Recog.*, pp. 5901–5910 (2020)
- [27] Hubara, I., Courbariaux, M., Soudry, D., El-Yaniv, R., Bengio, Y.: Binarized neural networks. *Adv. Neural Inform. Process. Syst.* **29** (2016)
- [28] Wetzstein, G., Ozcan, A., Gigan, S., Fan, S., Englund, D., Soljačić, M., Denz, C., Miller, D.A., Psaltis, D.: Inference in artificial intelligence with deep optics and photonics. *Nature* **588**(7836), 39–47 (2020)
- [29] Chang, J., Sitzmann, V., Dun, X., Heidrich, W., Wetzstein, G.: Hybrid optical-electronic convolutional neural networks with optimized diffractive optics for image classification. *Sci. Rep.* **8**(1), 12324 (2018)
- [30] Lin, X., Rivenson, Y., Yardimci, N.T., Veli, M., Luo, Y., Jarrahi, M., Ozcan, A.: All-optical machine learning using diffractive deep neural networks. *Science* **361**(6406), 1004–1008 (2018)

- [31] Wei, K., Li, X., Froech, J., Chakravarthula, P., Whitehead, J., Tseng, E., Majumdar, A., Heide, F.: Spatially varying nanophotonic neural networks. arXiv preprint arXiv:2308.03407 (2023)
- [32] Xu, J., Zheng, C.: Linear semantics in generative adversarial networks. In: IEEE Conf. Comput. Vis. Pattern Recog., pp. 9351–9360 (2021)
- [33] Collins, E., Bala, R., Price, B., Susstrunk, S.: Editing in style: Uncovering the local semantics of gans. In: IEEE Conf. Comput. Vis. Pattern Recog., pp. 5771–5780 (2020)
- [34] Shen, Y., Gu, J., Tang, X., Zhou, B.: Interpreting the latent space of gans for semantic face editing. In: IEEE Conf. Comput. Vis. Pattern Recog., pp. 9243–9252 (2020)
- [35] Karras, T., Aila, T., Laine, S., Lehtinen, J.: Progressive growing of GANs for improved quality, stability, and variation. In: Int. Conf. Learn. Represent. (2018)
- [36] McInnes, L., Healy, J., Melville, J.: Umap: Uniform manifold approximation and projection for dimension reduction. arXiv preprint arXiv:1802.03426 (2018)
- [37] Oord, A., Vinyals, O., Kavukcuoglu, K.: Neural Discrete Representation Learning (2018)
- [38] Razavi, A., Oord, A., Vinyals, O.: Generating Diverse High-Fidelity Images with VQ-VAE-2 (2019)
- [39] Mentzer, F., Minnen, D., Agustsson, E., Tschannen, M.: Finite scalar quantization: VQ-VAE made simple. In: The Twelfth International Conference on Learning Representations (2024)
- [40] Xu, Y., Lu, L., Saragadam, V., Kelly, K.F.: A compressive hyperspectral video

- imaging system using a single-pixel detector. *Nat. Commun.* **15**(1), 1456 (2024)
- [41] Lin, M., Ji, R., Xu, Z., Zhang, B., Chao, F., Lin, C.-W., Shao, L.: SiMaN: Sign-to-Magnitude Network Binarization (2022)
- [42] Abdal, R., Qin, Y., Wonka, P.: Image2StyleGAN: How to embed images into the StyleGAN latent space? In: *IEEE Conf. Comput. Vis. Pattern Recog.* (2019)
- [43] Creswell, A., Bharath, A.A.: Inverting the generator of a generative adversarial network. *IEEE transactions on neural networks and learning systems* **30**(7), 1967–1974 (2018)
- [44] Tov, O., Alaluf, Y., Nitzan, Y., Patashnik, O., Cohen-Or, D.: Designing an encoder for StyleGAN image manipulation. *ACM Trans. Graph.* **40**(4), 1–14 (2021)
- [45] Zhu, J., Shen, Y., Zhao, D., Zhou, B.: In-domain GAN inversion for real image editing. In: *Eur. Conf. Comput. Vis.* (2020)
- [46] Dinh, T.M., Tran, A.T., Nguyen, R., Hua, B.-S.: HyperInverter: Improving StyleGAN inversion via hypernetwork. In: *IEEE Conf. Comput. Vis. Pattern Recog.*, pp. 11389–11398 (2022)
- [47] Alaluf, Y., Tov, O., Mokady, R., Gal, R., Bermano, A.: HyperStyle: StyleGAN inversion with hypernetworks for real image editing. In: *IEEE Conf. Comput. Vis. Pattern Recog.*, pp. 18511–18521 (2022)
- [48] Kirillov, A., Mintun, E., Ravi, N., Mao, H., Rolland, C., Gustafson, L., Xiao, T., Whitehead, S., Berg, A.C., Lo, W.-Y., *et al.*: Segment anything. In: *IEEE Conf. Comput. Vis. Pattern Recog.*, pp. 4015–4026 (2023)
- [49] Liu, H., Dai, Z., So, D., Le, Q.V.: Pay attention to MLPs. *Adv. Neural Inform.*

Process. Syst. **34**, 9204–9215 (2021)

- [50] Deng, J., Guo, J., Xue, N., Zafeiriou, S.: Arcface: Additive angular margin loss for deep face recognition. In: IEEE Conf. Comput. Vis. Pattern Recog., pp. 4690–4699 (2019)
- [51] Zhang, R., Isola, P., Efros, A.A., Shechtman, E., Wang, O.: The unreasonable effectiveness of deep features as a perceptual metric. In: IEEE Conf. Comput. Vis. Pattern Recog., pp. 586–595 (2018)
- [52] Chen, X., Liang, C., Huang, D., Real, E., Wang, K., Pham, H., Dong, X., Luong, T., Hsieh, C.-J., Lu, Y., et al.: Symbolic discovery of optimization algorithms. *Advances in Neural Information Processing Systems* **36** (2024)
- [53] Zhang, M., Lucas, J., Ba, J., Hinton, G.E.: Lookahead optimizer: k steps forward, 1 step back. In: Wallach, H., Larochelle, H., Beygelzimer, A., Alché-Buc, F., Fox, E., Garnett, R. (eds.) *Adv. Neural Inform. Process. Syst.*, vol. 32. Curran Associates, Inc., ??? (2019)
- [54] Liu, L., Jiang, H., He, P., Chen, W., Liu, X., Gao, J., Han, J.: On the variance of the adaptive learning rate and beyond. In: *Int. Conf. Learn. Represent.* (2019)
- [55] Choi, Y., Uh, Y., Yoo, J., Ha, J.-W.: Stargan v2: Diverse image synthesis for multiple domains. In: *IEEE Conf. Comput. Vis. Pattern Recog.* (2020)
- [56] Zhang, J., Ghanem, B.: Ista-net: Interpretable optimization-inspired deep network for image compressive sensing. In: *IEEE Conf. Comput. Vis. Pattern Recog.*, pp. 1828–1837 (2018)
- [57] Mou, C., Wang, Q., Zhang, J.: Deep generalized unfolding networks for image restoration. In: *IEEE Conf. Comput. Vis. Pattern Recog.*, pp. 17399–17410 (2022)

- [58] Song, J., Mou, C., Wang, S., Ma, S., Zhang, J.: Optimization-inspired cross-attention transformer for compressive sensing. In: IEEE Conf. Comput. Vis. Pattern Recog., pp. 6174–6184 (2023)
- [59] Wang, P., Yuan, X.: Saunet: Spatial-attention unfolding network for image compressive sensing. In: Proceedings of the 31st ACM International Conference on Multimedia, pp. 5099–5108 (2023)
- [60] Higham, C.F., Murray-Smith, R., Padgett, M.J., Edgar, M.P.: Deep learning for real-time single-pixel video. *Sci. Rep.* **8**(1), 2369 (2018)
- [61] Zhang, Z., Wang, X., Zheng, G., Zhong, J.: Fast fourier single-pixel imaging via binary illumination. *Sci. Rep.* **7**(1), 12029 (2017)
- [62] Rizvi, S., Cao, J., Zhang, K., Hao, Q.: Improving imaging quality of real-time fourier single-pixel imaging via deep learning. *Sensors* **19**(19) (2019)
- [63] Yang, X., Jiang, P., Jiang, M., Xu, L., Wu, L., Yang, C., Zhang, W., Zhang, J., Zhang, Y.: High imaging quality of fourier single pixel imaging based on generative adversarial networks at low sampling rate. *Optics and Lasers in Engineering* **140**, 106533 (2021)
- [64] Rombach, R., Blattmann, A., Lorenz, D., Esser, P., Ommer, B.: High-Resolution Image Synthesis with Latent Diffusion Models (2021)
- [65] Ledig, C., Theis, L., Huszár, F., Caballero, J., Cunningham, A., Acosta, A., Aitken, A., Tejani, A., Totz, J., Wang, Z., *et al.*: Photo-realistic single image super-resolution using a generative adversarial network. In: IEEE Conf. Comput. Vis. Pattern Recog., pp. 4681–4690 (2017)
- [66] Blau, Y., Michaeli, T.: The perception-distortion tradeoff. In: IEEE Conf.

Comput. Vis. Pattern Recog., pp. 6228–6237 (2018)

- [67] Heusel, M., Ramsauer, H., Unterthiner, T., Nessler, B., Hochreiter, S.: Gans trained by a two time-scale update rule converge to a local nash equilibrium. *Adv. Neural Inform. Process. Syst.* **30** (2017)